

Topological corner modes in a brick lattice with nonsymmorphic symmetryYuhan Liu,^{1,2} Yuzhu Wang,^{1,3} Nai Chao Hu,^{1,4} Jun Yu Lin,^{1,5} Ching Hua Lee,^{6,7,*} and Xiao Zhang^{1,†}¹*Department of Physics, Sun Yat-sen University, Guangzhou 510275, China*²*Department of Physics, University of Chicago, Chicago, Illinois 60637, USA*³*Division of Physics and Applied Physics, Nanyang Technological University, Singapore 637371*⁴*Department of Physics, University of Texas at Austin, Austin, Texas 78712, USA*⁵*Department of Physics, The Chinese University of Hong Kong, Hong Kong, China*⁶*Institute of High Performance Computing, Singapore 138632*⁷*Department of Physics, National University of Singapore, Singapore 117542*

(Received 2 July 2019; accepted 29 June 2020; published 22 July 2020)

The quest for new realizations of higher-order topological system has garnered much recent attention. In this work, we propose a paradigmatic brick lattice model where corner modes require protection by nonsymmorphic symmetry in addition to two commuting mirror symmetries. Unlike the well-known square corner mode lattice, it has an odd number of occupied bands, which necessitates a different definition for the $\mathbb{Z}_2 \times \mathbb{Z}_2$ topological invariant. By studying both the quadrupolar polarization and effective edge model, our study culminates in a phase diagram containing two distinct topological regimes. Our brick lattice corner modes can be realized in an *RLC* circuit setup and detected via colossal “topoelectrical” resonances.

DOI: [10.1103/PhysRevB.102.035142](https://doi.org/10.1103/PhysRevB.102.035142)**I. INTRODUCTION**

In many topological condensed-matter systems, from quantum Hall gases [1–3] to topological insulators [4–12] and Weyl semimetals [13,13–18], the focus has been on protected modes at the boundary of a topological bulk. Such modes exist by virtue of nontrivial Wannier polarization, analogous to boundary charge accumulation from classical electric dipole polarization. But recently, this analogy has been further extended to quadrupolar or higher polarizations, where the intrinsic directionality of a multipole gives rise to enigmatic topological phenomena occurring only when *two or more* open boundaries are present [19]. In such systems, topologically protected “higher-order” corner modes can exist at the intersection of edges, even if the edges themselves do not host topological modes [20–25].

From a complementary viewpoint, these corner modes can also be inferred from special crystal symmetries, with their host lattices regarded as glorified topological crystalline insulators [23,25–31]. In the archetypal higher-order square lattice [19], the corner mode is protected by two noncommutable mirror symmetries that define a nontrivial mirror Chern number. As a slightly more sophisticated example, corner modes also exist in the breathing kagome lattice [32], where they are protected by three mirror symmetries. An advantage of viewing a higher-order phenomenon as a symmetry-protected topological order is that it does not presuppose the existence of a Fermi sea, unlike the viewpoint of nested Wannier polarization. As such, bona fide higher-order topological corner modes should exist in both classical and quantum lattices, even when higher-order polarization does not correspond to

any physical charge accumulation. Indeed, topological corner modes have been experimentally observed with relative ease in various classical photonic, mechanical, and electrical lattices [22,33,34], where couplings can be fine-tuned with precision.

Encouraged by these practical advances, we propose in this work a higher-order topological brick lattice with nonsymmorphic symmetry in addition to two commuting mirror symmetries [20], unlike the often-used square corner mode lattice which possesses C_4 rotational symmetry and two noncommuting mirror symmetries. More fundamentally, it has an odd instead of even number of occupied bands at half filling, which necessitates an alternative definition of its $\mathbb{Z}_2 \times \mathbb{Z}_2$ topological index distinct from well-studied models [19,35]. First, we begin by describing our brick lattice and providing numerical evidence for higher-order corner modes. Following that, we justify their robustness both in terms of a $\mathbb{Z}_2 \times \mathbb{Z}_2$ topological index and an edge Hamiltonian picture, with three distinct gapped phases illustrated in a phase diagram. Next, we discuss the consequences of breaking nonsymmorphic symmetry and thus the crucial mirror symmetries before finally proposing an experimental setup for detecting these brick lattice corner modes with circuit impedance measurements.

II. BRICK LATTICE MODEL AND CORNER MODES**A. Brick lattice structure and tight-binding Hamiltonian**

We study a brick lattice as shown in Fig. 1. The six sites in each unit cell are connected via various real hoppings, as described in Fig. 1(b). Notice that there are two inequivalent types of “bricks,” one which is wholly contained within a unit cell and one which straddles three unit cells and contains a possibly nonvanishing coupling t_3 through its width. Note that all couplings are meant to be properties of the lattice structure

* phylch@nus.edu.sg

† zhangxiao@mail.sysu.edu.cn

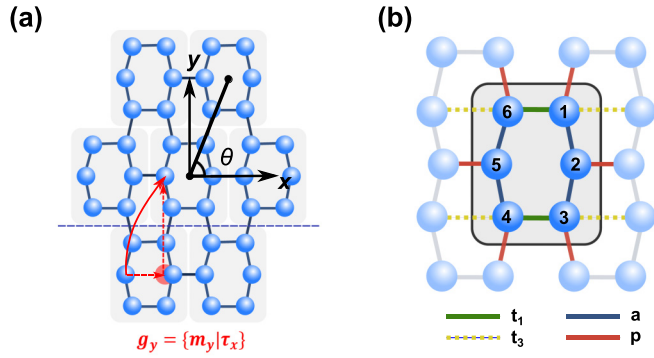


FIG. 1. (a) General structure of our brick lattice, which possesses commuting mirror-reflecting symmetries M_x and M_y about the x and y axes, as well as a nonsymmorphic symmetry $g_y = \{m_y | \tau_x\}$ (red arrow) consisting of a glide along half a unit cell (horizontal left arrow) and a reflection (vertical left arrow). Note that the reflection plane for g_y is the blue dashed line, not the x axis. (b) The sublattice basis and couplings t_1 , a , t_3 , p defining the brick Hamiltonian (1). There are two types of “bricks,” one contained with a single unit cell (shown) and the other straddling three neighboring unit cells, with an additional coupling t_3 across its width. t_3 and p always connect sites of adjacent unit cells.

and are unaffected by the lattice distortion angle θ . For this reason, our brick lattice is suitable for circuit implementation, as described later. In general, such a geometry-agnostic

$$H(k_1, k_2) = \begin{pmatrix} e & a & 0 & p e^{ik_1} & 0 & t_1 + t_3 e^{i(k_1+k_2)} \\ a & f & a & 0 & p e^{i(k_1+k_2)} & 0 \\ 0 & a & e & t_1 + t_3 e^{i(k_1+k_2)} & 0 & p e^{ik_2} \\ p e^{-ik_1} & 0 & t_1 + t_3 e^{-i(k_1+k_2)} & e & a & 0 \\ 0 & p e^{-i(k_1+k_2)} & 0 & a & f & a \\ t_1 + t_3 e^{-i(k_1+k_2)} & 0 & p e^{-ik_2} & 0 & a & e \end{pmatrix}, \quad (1)$$

with on-site energies e and f at the corners and midpoints of each brick, respectively. k_1, k_2 are related to the lattice momenta k_x, k_y via $k_1 = k_x \cos \theta + k_y \sin \theta$, $k_2 = k_x \cos \theta - k_y \sin \theta$, such that θ indeed never appears explicitly. Since higher-order topological phenomena are essentially mathematical properties of the lattice rather than of the particles inhabiting it, our results will be equally valid even if $H(k_1, k_2)$ is interpreted as a lattice Laplacian or any other linear operator on the lattice graph.

B. Band structure and corner modes

We next sequentially present the band structure and eigenmodes of our brick Hamiltonian under periodic and single and double open boundary conditions (PBCs and single and double OBCs) to elucidate how exactly the corner modes emerge.

To present various possible contrasting scenarios, we shall consider three sets of parameters, as illustrated in the top row of Fig. 2:

property is useful for lattice model engineering, where desired properties can be designed through universal complex analytic properties that are embedded in the graph structure [36–39], not the geometric structure of the lattice.

As we can see in Fig. 1(a), the brick lattice possesses two commuting mirror symmetries M_x and M_y about the x and y axes, as well as the nonsymmorphic (glide reflection) symmetry $g_y = \{m_y | \tau_x\}$. Specifically, the lattice is mapped onto itself when translated along half a unit cell (τ_x , red dashed arrow) and then reflected along the mirror plane (m_y , blue dashed line). By examining how one lattice point is mapped in the successive actions of $M_x g_y$ and $g_y M_x$, it is easy to see g_y does not commute with M_x on the lattice level. In fact, noncommuting is a general feature of glide symmetry [40], which is important because having two commuting mirror symmetries is not sufficient to realize the quadruple [19]. When $t_1 = a$ and $t_3 = 0$, our brick lattice possesses the same C_6 rotational symmetry as the corner mode lattice of [21], but as we shall show, the corner mode behavior can persist far beyond this limit and hence does not require C_6 rotational symmetry at all. Indeed, nonsymmorphic symmetry has been known to protect various interesting topological features, from tilted Dirac cones to surface states with Möbius twists [40–45].

In the basis of sublattices 1 to 6 illustrated in Fig. 1(b), the couplings are contained in an effective Hamiltonian,

$$\begin{aligned} \text{Case A: } & p = -5.0, t_1 = -1.0, t_3 = -0.1, a = -1.0, \\ \text{Case B: } & p = -0.5, t_1 = -1.0, t_3 = -0.1, a = -1.0, \\ \text{Case C: } & p = -4.0, t_1 = -1.0, t_3 = -7.0, a = -1.0. \end{aligned} \quad (2)$$

Case A contains much stronger couplings across unit cells than case B. Case C is somewhat similar to case A, but with much stronger t_3 -type couplings across the widths of bricks that straddle unit cells. Henceforth, we shall also set the on-site energies e and f to zero, so that the corner modes can be pinned at zero energy ($\omega = 0$).

First, we examine the bulk (PBC) band structure of the brick lattice. In all three cases, a gap clearly separates the upper three bands from the lower three bands (Fig. 2, middle row), allowing unambiguous topological characterization of potential midgap modes.

Next, we introduce a boundary perpendicular to the x axis, such that k_2 remains a good “quantum number” (Fig. 2, bottom row). While edge modes (red) now appear in cases A and

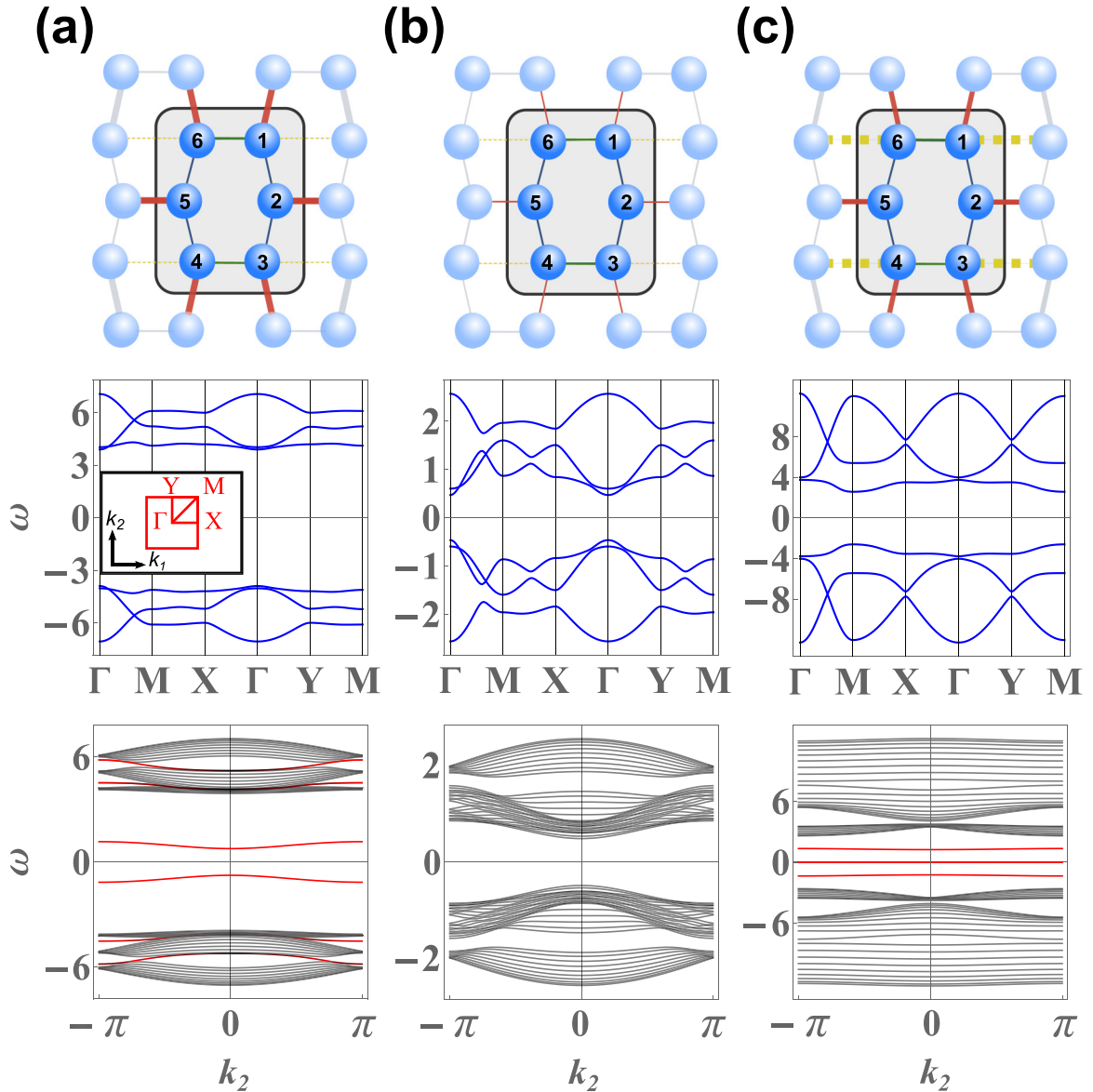


FIG. 2. Bulk and edge spectra of our brick lattice Hamiltonian, with columns in (a) to (c) corresponding to parameters given by cases A to C (3). Top row: Lattice couplings for each case, colored according to Fig. 1(b) with thicknesses proportional to coupling magnitude. Middle row: PBC band structures with well-defined zero-energy gaps for all three cases. Bottom row: Spectra under a single OBC along the x direction, with bulk (edge) modes colored black (red). All cases have trivial first-order topology: The edge modes of cases A and C do not traverse the gap, and case B does not even have edge modes.

C, they do not traverse the gap. This indicates constant first-order polarization and hence trivial *first-order* \mathbb{Z}_2 topology, which is expected from our simple lattice structure devoid of effective pseudospin-orbit coupling [46,47].

What is interesting is that, after taking OBCs in both the x and y directions (double OBCs), second-order topological corner modes can still appear even though the edge modes with a single OBC do not exhibit topological polarization. As shown in Fig. 3, such corner modes occur in cases A and C, but not B. In case A [Fig. 3(a)], we observe a twofold-degenerate density of states (DOS) peak at energy $\omega = 0$, with each copy corresponding to a corner mode plotted in the lower left panel. Other DOS peaks away from zero energy but within the bulk gap correspond to edge modes. Neither corner nor edge modes exist in case B [Fig. 3(b)], which exhibits

only bulk modes. Indeed, without edge modes from single OBCs, corner modes cannot possibly appear when another open boundary is introduced. Case C [Fig. 3(c)] is somewhat similar to case A, but its zero energy modes are not isolated from the other modes and hence do not form well-defined corner modes. In the following, we shall explain and substantiate these observations through topological arguments.

III. TOPOLOGICAL CHARACTERIZATION OF CORNER MODES

We now briefly recap the theory of higher-order topological polarization before describing a $\mathbb{Z}_2 \times \mathbb{Z}_2$ topological classification of our brick lattice corner modes different from that in the existing literature.

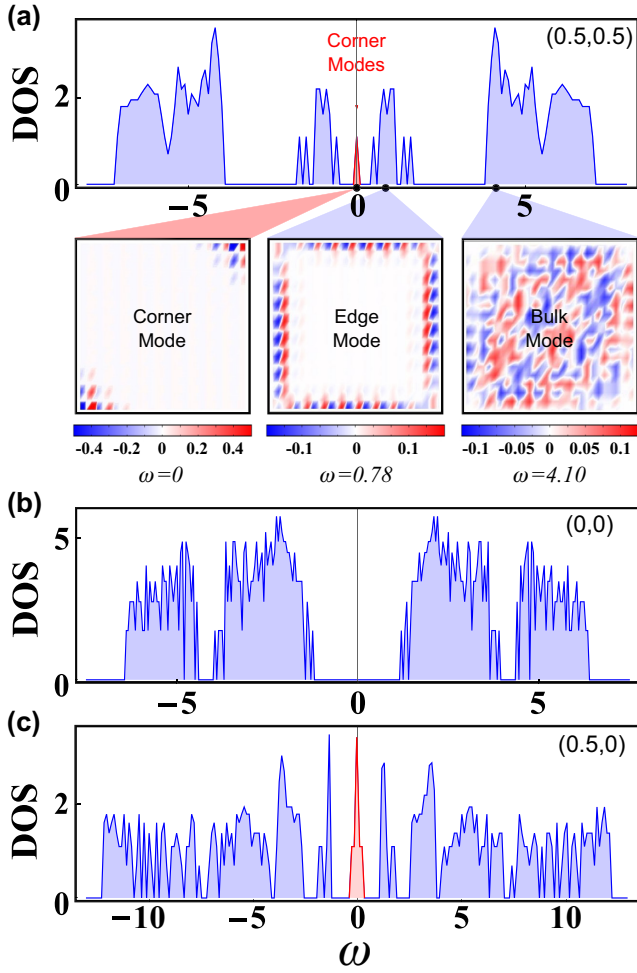


FIG. 3. Double OBC density of states (DOS) for cases (a) A, (b) B, and (c) C as a function of energy ω , calculated on a finite lattice with 10×10 unit cells. Midgap modes exist within the bulk gap for cases A and C, but only case A has well-separated doubly degenerate corner zero modes. Its spatial wave function distribution is illustrated at frequencies $\omega = 0$ (left), $\omega = 0.78$ (middle), and $\omega = 4.10$ (right), where it is dominated by corner, edge, and bulk modes, respectively. The DOS vertical axis is plotted on a logarithmic scale.

A. First-order polarization

First, we introduce the notion of topological (Wannier) polarization. Consider a two-dimensional Hamiltonian $H(k_1, k_2)$ with OBCs in the x direction, such that its eigenstates $|\Psi(k_2)\rangle$ are indexed by $k_2 \in [0, 2\pi)$, which remains a good quantum number. Of central importance is the projected periodic position operator

$$\hat{X}_P(k_2) = \hat{P}(k_2) e^{2\pi i \hat{x}/N_x} \hat{P}(k_2), \quad (3)$$

where \hat{x} is the usual position operator, $\hat{P}(k_2) = |\Psi(k_2)\rangle\langle\Psi(k_2)|$ is the projection onto a chosen $|\Psi(k_2)\rangle$ band, and N_x is the number of unit cells along the x direction. The *first-order* polarization $\langle x(k_2) \rangle$ is given by the rescaled phase of the eigenvalues of $\hat{X}_P(k_2)$:

$$\langle x(k_2) \rangle = \frac{N_x}{2\pi} \text{Im} \ln \langle \Psi(k_2) | e^{2\pi i \hat{x}/N_x} | \Psi(k_2) \rangle. \quad (4)$$

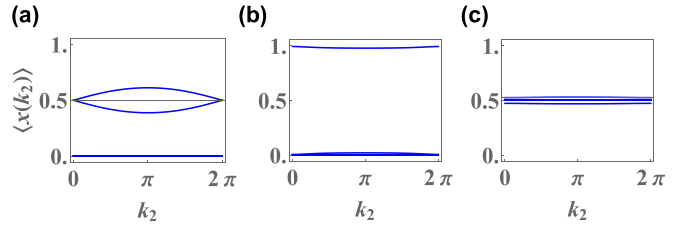


FIG. 4. Evolution of Wannier centers $\langle x(k_2) \rangle$ for cases (a) A, (b), and (c) C over one period of k_2 . For all cases, there is no partner switching, and a dispersionless trajectory always exists. Cases A and C, which contain edge modes, also have Wannier centers hovering around 0.5. These first-order polarizations should not be confused with the second-order polarizations p_y^j , which define the second-order $\mathbb{Z}_2 \times \mathbb{Z}_2$ via Eq. (7).

For a Hamiltonian with b bands, there exist bN_x eigenvalues of $X_P(k_2)$, but only b of them are independent: The rest are translated by a phase of $2\pi/N_x$ and as such correspond to the same polarization [48,49] $\langle x(k_2) \rangle$.

Physically, the polarization is the center-of-mass position of its corresponding $\hat{X}_P(k_2)$ eigenstate, which is also a maximally localized Wannier function for any given k_2 [50–53]. Hence, it is also called the Wannier center. For a Fermi gas of electrons, the polarization tells us, through the Laughlin gauge argument, how charge within the occupied Fermi sea is inevitably topologically “pumped” by an electric field that translates k_2 . Numerically, the Wannier centers can be computed via the Wilson loop operator $W_{k_1+2\pi \leftarrow k_1}$, as detailed in Sec. A1.

In our brick lattice with time-reversal symmetry, the band topology is characterized by a \mathbb{Z}_2 invariant [4,6,52] which can be read from the spectral flow of the polarization [52]. Specifically, the \mathbb{Z}_2 index is trivial or nontrivial depending on whether the $\langle x(k_2) \rangle$ eigenvalues “switch partners” as k_2 varies over half a period, i.e., from one time-reversal-invariant point to the other. This is equivalent to checking whether a particular $\langle x(k_2) \rangle$ Wannier center trajectory crosses an arbitrary line parallel to the k_2 axis an even or odd number of times as k_2 varies over a period.

In general, the polarization flow bears a one-to-one correspondence with the energy spectral flow: for each pair of Wannier centers that switch partners, there also exists a pair of gapless edge modes that switch partners and traverse the bulk gap. In particular, a gapped OBC spectrum can contain only $\mathbb{Z}_2 = 0$ bulk bands, as in all of the cases plotted in the bottom row of Fig. 2. They can possess either edge modes that do not traverse the gap (cases A and C) or no edge modes at all (case B). These behaviors are reflected in their polarization trajectories, shown in Fig. 4. While none of them exhibit partner switching and are hence all \mathbb{Z}_2 trivial, cases A and C both possess polarizations that fluctuate about 0.5, indicative of midgap localization tendencies of their respective OBC edge modes.

B. Second-order polarization and $\mathbb{Z}_2 \times \mathbb{Z}_2$ classification of corner modes

To understand how topological corner modes can arise from trivial single OBC \mathbb{Z}_2 edge modes, we now introduce

the concept of second-order quadrupole polarization [19]. The main idea is to use the gapped (first-order) Wannier bands as the “bulk” bands of a new effective system and apply the machinery of Wannier polarization on it to obtain the *second-order* polarization properties of the original system. This procedure can, of course, be repeated ad infinitum to obtain higher-order polarizations in a higher-dimension system, although we shall stop at the second order in this work since the brick lattice is two-dimensional.

More concretely, one divides the set of Wannier centers $\langle x(k_2) \rangle$ into mutually nonintersecting (gapped) sectors, such that intersecting Wannier centers combine to form a single sector [19,35]. Just like gapped bands, each sector is well separated from the others and can thus be unambiguously characterized topologically. For each j th Wannier center, $j = 1, \dots, N_F$, where N_F is the number of occupied bands, we can define an effective second-order “bulk” state $|\omega_{x,k}^j\rangle$ in terms of its corresponding Wannier function:

$$|\omega_x^j(\mathbf{k})\rangle = \sum_{n=1}^{N_F} |u_k\rangle [v_{x,k_2}^j]^n, \quad (5)$$

where $[v_{x,k_2}^j]^n$ is the n th component of the j th Wannier function in the basis of occupied bands and $|u_k\rangle$ is the n th Bloch state. In analogy to the first-order polarization, one can thus compute a *second-order* polarization

$$p_y^j = -\frac{i}{2\pi} \frac{1}{N_x} \sum_{k_1} \ln(\tilde{W}_{y,k_1}^j) \quad (6)$$

from the *nested* Wilson loop operator \tilde{W}_{y,k_1}^j formed from $|\omega_x^j(\mathbf{k})\rangle$, as detailed in Sec. A1. The y subscript in p_y^j indicates that it refers to the y -direction nested polarization of open boundary condition in the x direction (x -OBC) Wannier functions; p_x^j does not necessarily equal p_y^j unless a mirror symmetry maps one boundary to the other.

The topological class of a second-order (double OBC) system is given by the set of \mathbb{Z}_2 numbers associated with the Wannier sectors. In the well-studied square corner mode lattice [19,35] with $N_F = 2$ gapped occupied edge bands at half filling, there are two Wannier sectors, and a $\mathbb{Z}_2 \times \mathbb{Z}_2$ classification can be defined [54]. But in our model with $N_F = 3$ occupied bands at half filling, a *different* [19] $\mathbb{Z}_2 \times \mathbb{Z}_2$ classification must be defined. Since there is already a dispersionless Wannier center due to odd N_F and M_x symmetry, we shall let it be in its own Wannier sector with corresponding second-order polarization p_y^1 (a flat trajectory in each plot of Fig. 4). The other two Wannier bands may generically intersect and will be taken to form the other sector. Hence, we define, for our brick lattice, a $\mathbb{Z}_2 \times \mathbb{Z}_2$ topological index,

$$(\mu, \nu) = (p_y^1, p_y^2 + p_y^3). \quad (7)$$

A phase diagram for the brick lattice is shown in Fig. 5 for fixed intra-unit-cell couplings $a = t_1 = -1$ and variable inter-unit-cell couplings p and t_3 . Case A is deep within the $(\mu, \nu) = (0.5, 0.5)$ region with $p_y^1 = 0.5$ and $p_y^2 + p_y^3 = 0.5$ and hosts two distinct degenerate corner modes. Case B, which essentially consists of islands dominated by intra-unit-cell couplings a, t , is nontopological as expected, with neither edge (Fig. 2) nor corner modes. Case C belongs to the more

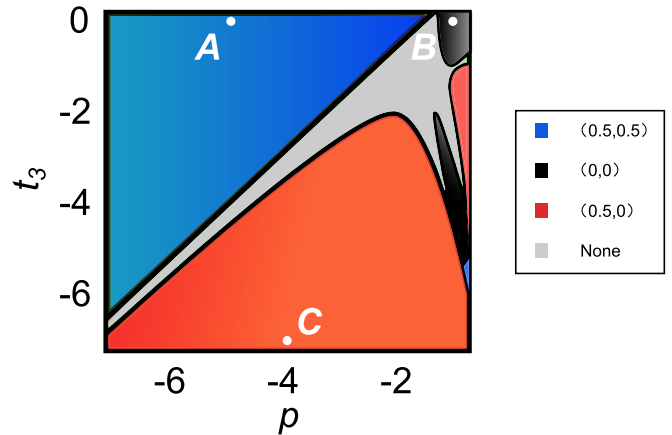


FIG. 5. Topological phase diagram for our brick lattice, with cases A to C each corresponding to a different $(\mu, \nu) \in \mathbb{Z}_2 \times \mathbb{Z}_2$ class. Interestingly, the trivial $(0,0)$ phase occupies a relatively small region and is separated from the two distinct topological phases via a somewhat larger gapless regime (gray), where the topology is not well defined. Generally, $|p| > |t_3|$ favors the blue $(0.5,0.5)$ nontrivial phase (and vice versa for $|p| < |t_3|$), illustrating the competition between width and edge couplings across the unit cells.

enigmatic $(0.5,0)$ phase, which is encouraged by a dominant t_3 . To gain some intuition, consider the extreme limit of large $|t_3|$ and small $|p|$, where the brick lattice essentially splits into weakly coupled one-dimensional (1D) Su-Schrieffer-Heeger (SSH) ladders with strong coupling t_3 and weak coupling t_1 and relatively weak “rungs” composed of two successive a couplings (Fig. 1). In this quasi-1D limit, corner modes obviously should not exist, although a continuum of boundary modes at the ends of each ladder still gives rise to $1/2$ polarization. In this sense, the $(0.5,0)$ phase can be regarded as the “horizontal half” of the $(0.5,0.5)$ phase, although the above analogy quickly becomes inaccurate away from the extreme limit. Finally, we note that the various topological phases are usually not adjacent to each other: To transform from one topological phase to another, the requisite band gap closure may last indefinitely long, i.e., if the parameters are transformed along the gray strip $t_3 \approx p$.

IV. CORNER MODES FROM THE EFFECTIVE 1D EDGE PICTURE

To more intuitively understand the origin of the corner modes, we now consider cases where the corner mode can be largely explained with a 1D edge picture. Instead of invoking the rather abstract nested polarizations, we attempt to visualize corner modes as the intersections of the boundary modes of 1D SSH-like edges.

The double OBCs in our brick lattice produce armchairlike edges in both directions, as shown in Fig. 6. Evidently, the edgmost couplings form SSH-like chains along each edge, each with four sites per unit cell:

$$H_{\text{edge}}(k) = \begin{pmatrix} 0 & t_1 & 0 & p e^{-ik} \\ t_1 & 0 & a & 0 \\ 0 & a & 0 & a \\ p e^{ik} & 0 & a & 0 \end{pmatrix}. \quad (8)$$

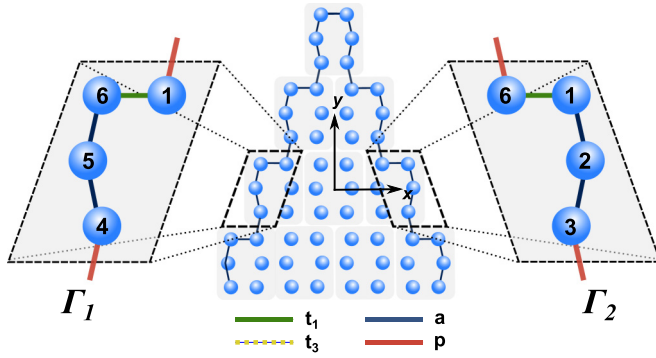


FIG. 6. One-dimensional armchair chains Γ_1 and Γ_2 at the edges of both boundaries, which are equivalent due to lattice mirror symmetry. The four inequivalent atoms in their unit cells couple according to H_{edge} [Eq. (8)], whose gap closure at $p = t_1$ for $t_3 = 0$, $a = -1$ agrees with the phase diagram for the *full* brick lattice (Fig. 5).

In chains Γ_1 and Γ_2 as shown, the basis in H_{edge} is taken to be sites 1,6,5,4 and 6,1,2,3, respectively.

Like the well-known SSH model, this four-band model contains topological zero modes when the inter-unit-cell coupling p is larger than the intra-unit-cell coupling t_1 . This can be seen from the analytic expression of its eigenenergies $\omega^2 = a^2 + Q^2 \pm \sqrt{a^4 + Q^4 + 2a^2 p t_1 \cos k}$, with $Q^2 = (p^2 + t_1^2)/2$, which gives the *only* gap closure and hence the possible topological phase transition at $t = p_1$. In other words, the a intra-unit-cell couplings are “spectators” that play no part in determining the topology and leave behind an SSH-like dimerization mechanism for topological boundary modes. Setting $t_1 = a = -1$ as before, we see that the topological phase transition point $p = a = -1$ for H_{edge} indeed agrees with the phase diagram of the full brick lattice in Fig. 5. Indeed, as shown in Fig. 7(c), its DOS also agrees qualitatively with that of the full brick lattice in Fig. 3, with corner modes comprising superposed SSH-like boundary modes from both chains Γ_1 and Γ_2 . Note that this admittedly rudimentary edge model completely ignores the effects of coupling between adjacent chains and thus cannot predict the effects of t_3 . A more detailed analysis of these neighboring couplings may provide intuition for the entire phase diagram, as has been done for the square corner mode model [55].

V. EFFECT OF BREAKING NONSYMMORPHIC SYMMETRY

As previously emphasized, a hallmark of our brick lattice is its nonsymmorphic symmetry in addition to its two commuting mirror symmetries. Below, we show that with our lattice structure, the nonsymmorphic symmetry $g_y = \{m_y | \tau_x\}$, if broken in certain ways, also leads to the disappearance of well-defined corner zero modes.

As illustrated in Fig. 8(a), we break the nonsymmorphic symmetry $g_y = \{m_y | \tau_x\}$ by removing the t_1 couplings of alternate original unit cells (green \rightarrow white), i.e., sites 1,6 and

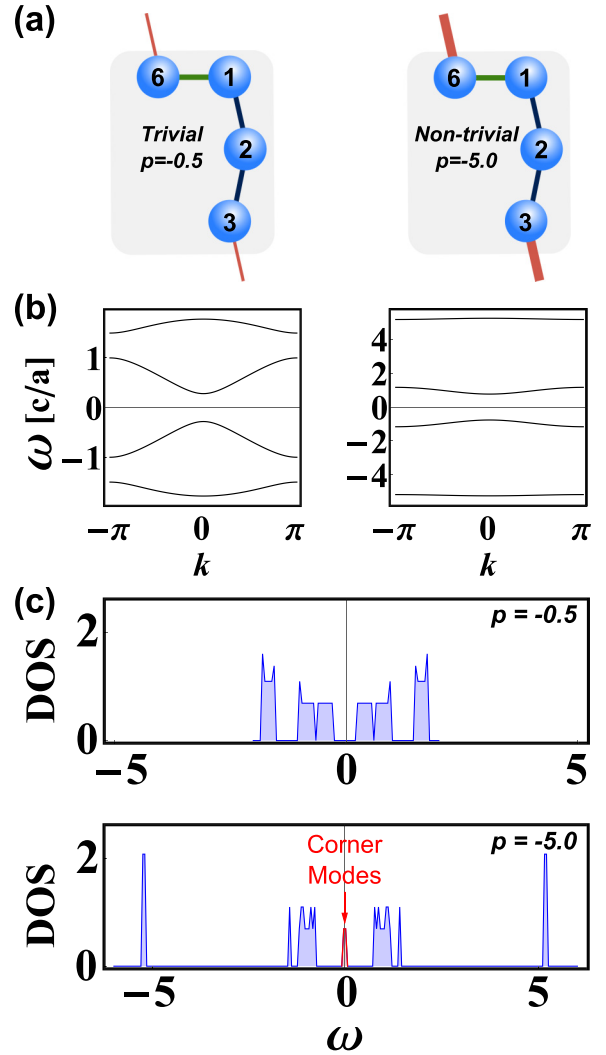


FIG. 7. (a) Illustration of one-dimensional armchair chains at the edges (we take Γ_2 for an example) with different coupling parameters p . (b) The bulk modes and (c) DOS plots reveal the existence of corner modes in the one-dimensional armchair chains with topologically nontrivial p , with qualitative agreement with the DOS of the full brick lattice in Fig. 3.

3,4 are no longer coupled by t_1 . Thus, the mirror symmetries M_x and M_y are obviously preserved since the t_1 's are removed symmetrically within each unit cell. However, nonsymmorphic symmetry is broken because site 12 no longer maps identically to site 4 and vice versa for site 11 to site 5, etc. In Figs. 8(b) and 8(c), we no longer observe well-defined zero modes in the DOS. This destruction of the corner zero modes is expected from the previous effective edge picture, which gives two inequivalent SSH-like chains that do not “dimerize” in the same way.

VI. EXPERIMENTAL PROPOSAL VIA RLC CIRCUITS

Finally, we briefly discuss how to experimentally realize a brick lattice and measure its corner modes. Of various possible platforms in photonic, mechanical, and acoustic systems

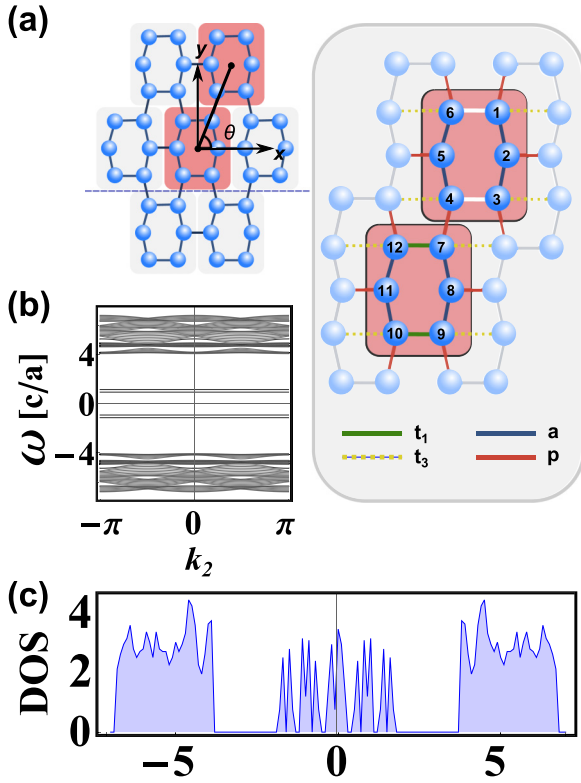


FIG. 8. (a) Illustration of a modification to the brick lattice that breaks the nonsymmorphic symmetry g_y but preserves the mirror symmetries M_x and M_y . Each unit cell now consists of 12 sites, with half of the t_1 (green) couplings removed. (b) Single OBC spectrum and (c) double OBC DOS, showing the absence of isolated zero-energy topological modes.

$$J(k_1, k_2; \omega) = -i\omega \begin{pmatrix} e' & a & 0 & p e^{ik_1} & 0 & t_1 + t_3 e^{i(k_1+k_2)} \\ a & f' & a & 0 & p e^{i(k_1+k_2)} & 0 \\ 0 & a & e' & t_1 + t_3 e^{i(k_1+k_2)} & 0 & p e^{ik_2} \\ p e^{-ik_1} & 0 & t_1 + t_3 e^{-i(k_1+k_2)} & e' & a & 0 \\ 0 & p e^{-i(k_1+k_2)} & 0 & a & f' & a \\ t_1 + t_3 e^{-i(k_1+k_2)} & 0 & p e^{-ik_2} & 0 & a & e' \end{pmatrix}, \quad (10)$$

with $e' = \frac{1}{\omega^2 L_e} - a - p - t_1 - t_3$ and $f' = \frac{1}{\omega^2 L_f} - 2a - p$. By tweaking L_e and L_f , one can easily make them equal, such that the on-site admittances become a constant shift of the Laplacian eigenvalues, analogous to the chemical potential.

To detect the corner modes, one measures the impedance [61]

$$\begin{aligned} Z_{ab}(\omega) &= \frac{V_a - V_b}{I_0} \\ &= \sum_n \frac{|\phi_n(a) - \phi_n(b)|^2}{j_n(\omega)} \end{aligned} \quad (11)$$

between two nodes a and b with respect to a current I_0 entering from a and leaving from b . The second line is defined via $J_{ab}(\omega) = \sum_n j_n(\omega) |\phi_n(a)\rangle \langle \phi_n(b)|$, the expansion of the Laplacian into its eigenmodes. Most salient from

[34,56,57], an RLC circuit realization is arguably the least challenging, with an experimental smoking gun being easily performed impedance experiments [22,47,58–60]. Since this approach is already quite mature, with a related corner mode circuit experiment performed last year [22], we shall refer the reader to various excellent references for most of the details [46,61–63].

In a circuit, the physics are most directly described via Kirchhoff's law, which can be put into a matrix form:

$$I_a(\omega) = \sum_b J_{ab}(\omega) V_b(\omega), \quad (9)$$

where $I_a(\omega)$ and $V_b(\omega)$ are the frequency-space net input current and electrical potential at nodes a and b , respectively. $J_{ab}(\omega)$ is the circuit Laplacian that captures the circuit behavior. For our purposes, $J_{ab}(\omega)$ will replace the Hamiltonian, such that the DOS and energy spectrum now refer to those of the Laplacian.

To realize our brick lattice [Eq. (1)] with a Laplacian, one simply substitutes each coupling by a capacitor proportional to its value, such that a coupling $H_{jk} = -p$, $p > 0$, becomes the admittance contributions $J_{jj}(\omega) = J_{kk}(\omega) = -i\omega p$ and $J_{jk}(\omega) = J_{kj}(\omega) = i\omega p$, with ω being the AC frequency. To independently control the on-site couplings, we also connect grounded inductors L_e or L_f to each site, such that they acquire on-site admittance contributions of $(i\omega L_e)^{-1}$ or $(i\omega L_f)^{-1}$. Made out of capacitors of capacitances a , p , t_1 , t_3 and the grounding inductors described below, the brick circuit possesses a Laplacian of the form

this key expression is that zero modes $j_n(\omega) \approx 0$ give rise to large divergences, which are also known as topoelectrical resonances. By measuring the impedance between two points near a corner, corner zero modes can be easily identified as large impedances or resonances.

VII. CONCLUSION

Compared to well-known higher-order lattices like the square corner mode lattice, our brick lattice is fundamentally different in two ways: Its corner zero modes requires nonsymmorphic symmetry in addition to two mirror symmetries, and it has an odd number of occupied bands, which necessitates a different definition of the $\mathbb{Z}_2 \times \mathbb{Z}_2$ topological invariant. In addition to trivial gapped and gapless phases, we also uncovered two distinct topological phases: $(\mu, \nu) = (0.5, 0.5)$, with distinct corner modes, and $(\mu, \nu) = (0.5, 0)$, hosting

continuum boundary modes and adiabatically connected to weakly coupled SSH ladders. We conclude our work by describing how brick lattice corner modes can be realized and easily detected in a circuit setup, a platform that has proved to be experimentally accessible and amenable to interesting nonlinear, non-Hermitian, or Floquet generalizations [59,64–67].

ACKNOWLEDGMENTS

C.H.L. thanks L. Li for discussions. X.Z. is supported by the National Natural Science Foundation of China (Grant No. 11874431), the National Key R&D Program of China (Grant No. 2018YFA0306800), and the Guangdong Science and Technology Innovation Youth Talent Program (Grant No. 2016TQ03X688).

Y.L. and Y.W. contributed equally to this work.

APPENDIX A: THE WILSON LOOP

1. Wilson loop over occupied energy bands

In the main text, we have alluded to using the Wilson loop to compute the Wannier center evolution of a given Hamiltonian. Here we show a detailed description of the procedure, mainly following [52,53] and the supplement of [19]. Fixing k_2 such that the system is effectively one-dimensional, the projection operator $\hat{P}(k_2)$ of the occupied bands (from $n = 1$ to $n = N_F$) is

$$\hat{P}(k_2) = \sum_{k_1} \sum_{n=1}^{N_F} |\Psi_n(k)\rangle \langle \Psi_n(k)| = \sum_{k_1} |k\rangle \langle k| \otimes \hat{P}(k), \quad (\text{A1})$$

where $\hat{P}(k) = \sum_{n=1}^{N_F} |u_n(k)\rangle \langle u_n(k)|$. We next write down the unitary periodic position operator of the occupied bands, defined as

$$\hat{X}_P(k_2) = \hat{P}(k_2) \hat{X} \hat{P}(k_2), \quad (\text{A2})$$

where $\delta_k = 2\pi/N_x$ and $\hat{X} = e^{i\delta_k \hat{x}}$. Using $\langle \Psi_{n'}(k') | \hat{X} | \Psi_n(k) \rangle = \delta_{k+\delta_k, k'} \langle u_{n'}(k+\delta_k) | u_n(k) \rangle$ and substituting the above definition of $\hat{P}(k_2)$, we get

$$\hat{X}_P(k_2) = \sum_{k_1} \sum_{n', n=1}^{N_F} \langle u_{n'}(k+\delta_k) | u_n(k) \rangle \cdot |\Psi_{n'}(k+\delta k)\rangle \langle \Psi_n(k)|. \quad (\text{A3})$$

The summation over k has N_x terms, so the above operator can be expressed as an $N_F \times N_x$ matrix. If we define matrix G_k with component $[G_k]^{mn} = \langle u_n(k+\delta k) | u_m(k) \rangle$, it is not unitary because N_x is finite. To facilitate the numerical computation, we can perform the singular-value decomposition $G = UDV^\dagger$, where D is a diagonal matrix. If we define $F_k = UV^\dagger$, we get a unitary matrix which equals G_k in the thermodynamic limit, and we can write the operator \hat{X}_P in the thermodynamic limit case, under the $N_x \times N_F$ basis of $|\Psi_n(k)\rangle$:

$$\hat{X}_P(k_2) = \begin{pmatrix} 0 & 0 & 0 & \cdots & F_{k_N} \\ F_{k_1} & 0 & 0 & \cdots & 0 \\ 0 & F_{k_2} & 0 & \cdots & 0 \\ \vdots & \vdots & \vdots & \ddots & \vdots \\ 0 & 0 & 0 & \cdots & 0 \end{pmatrix}, \quad (\text{A4})$$

where $k_i = 0, k_{ii} = \delta k, \dots, k_N = \delta k(N_x - 1)$. Each matrix F is an $N_F \times N_F$ matrix. We write its eigenvector in terms of a $1 \times N_F$ block, namely,

$$\hat{X}_P \begin{pmatrix} v_{k_i} \\ v_{k_{ii}} \\ v_{k_{iii}} \\ \vdots \\ v_{k_N} \end{pmatrix}^j = E^j \begin{pmatrix} v_{k_i} \\ v_{k_{ii}} \\ v_{k_{iii}} \\ \vdots \\ v_{k_N} \end{pmatrix}. \quad (\text{A5})$$

The Wilson loop operator is defined as

$$W_{k+2\pi \leftarrow k} = F_{k+2\pi-\delta k} F_{k+2\pi-2\delta k} \cdots F_{k+\delta k} F_k. \quad (\text{A6})$$

By recursively applying the above equations to the eigenvector, we can derive the eigenvalue equation

$$W_{k_1+2\pi \leftarrow k_1} |v_{x,k}^j\rangle = (E^j)^{N_x} |v_{x,k}^j\rangle. \quad (\text{A7})$$

Here we write $|v_k^j\rangle$ as $|v_{x,k}^j\rangle$ to denote that the Wilson loop is taken along \hat{x} . It should be noticed that although the eigenstates $|v_k^j\rangle$ are different for different k , their eigenvalues are the same for a fixed k_2 . So if we care about only the eigenvalue, we can choose any k_1 to be the starting point of the Wilson loop. If we have N_F occupied bands, we can solve Eq. (A7) to get N_F different E^j . Looking back at the definition of \hat{X}_P in Eq. (A2), we can relate the phase of $(E^j)^{N_x}$ to $\langle x \rangle$ as in the main text.

Figure 4 of the main text plots the phase of $(E^j)^{N_x}$ of different k_2 . Since the Hamiltonian possesses pseudo-time-reversal symmetry, we need to plot k_2 from only zero to π , with the part from $-\pi$ to zero related by symmetry.

2. Nested Wilson loop over Wannier sectors

We define the Wannier basis

$$|\omega_x^j(\mathbf{k})\rangle = \sum_{n=1}^{N_F} |u_n^n\rangle [v_{x,k}^j]^n \quad (\text{A8})$$

as in the main text and use it to calculate the nested Wilson loop \tilde{W}_{y,k_1} in a way similar to the (first-order) Wilson loop:

$$\tilde{W}_{y,k_1}^j = \tilde{W}_{k_2+2\pi \leftarrow k_2}^j = \tilde{F}_{k_2+2\pi-\delta k}^j \tilde{F}_{k_2+2\pi-2\delta k}^j \cdots \tilde{F}_{k_2+\delta k}^j \tilde{F}_{k_2}^j, \quad (\text{A9})$$

where $[\tilde{F}_{k_2}^j]^{mn} = \langle \omega_x^{j,m}(k_1, k_2 + \delta k) | \omega_x^{j,n}(k_1, k_2) \rangle$, which is independent of x .

APPENDIX B: SYMMETRY OF THE HAMILTONIAN

1. Chiral symmetry

In the SSH model with two sublattice degrees of freedom, the chiral symmetry is expressed as

$$\sigma_z H(k) \sigma_z = -H(k). \quad (\text{B1})$$

Here we have six sublattices, so by analogy we can define a new s'_z :

$$s'_z = \begin{pmatrix} 1 & 0 & 0 & 0 & 0 & 0 \\ 0 & -1 & 0 & 0 & 0 & 0 \\ 0 & 0 & 1 & 0 & 0 & 0 \\ 0 & 0 & 0 & -1 & 0 & 0 \\ 0 & 0 & 0 & 0 & 1 & 0 \\ 0 & 0 & 0 & 0 & 0 & -1 \end{pmatrix}. \quad (\text{B2})$$

In fact, this is the only way to define s'_z , up to an overall minus. The Hamiltonian has chiral symmetry when all the diagonal terms are zero. To break the chiral symmetry, we can add on-site energy terms, for example, by

$$\text{diag}(e \ f \ e \ e \ f \ e). \quad (\text{B3})$$

We take other parameters to be $p = -5$, $t_1 = -1$, $t_3 = -0.1$, $a = -1.0$, which is the parameter of phase A. By taking $e = 0.05$, $f = 0$, we observe the two zero modes separate into two energies $E = \pm 0.05$, but they are still well localized at the corners. If we take $e = 0$, $f = 0.02$, although chiral symmetry is broken, the two zero modes are still degenerate and at zero energy. To sum up, chiral symmetry is needed for the two corner modes to be degenerate and located at zero energy.

2. Spatial symmetry

Note that we make the substitution $H_0(k_x, k_y) = H(k_x \cos \theta + k_y \sin \theta, k_x \cos \theta - k_y \sin \theta)$.

Mirror symmetry m_y is

$$m_y = \begin{pmatrix} 0 & 0 & 1 & 0 & 0 & 0 \\ 0 & 1 & 0 & 0 & 0 & 0 \\ 1 & 0 & 0 & 0 & 0 & 0 \\ 0 & 0 & 0 & 0 & 0 & 1 \\ 0 & 0 & 0 & 0 & 1 & 0 \\ 0 & 0 & 0 & 1 & 0 & 0 \end{pmatrix}, \quad (\text{B4})$$

$$m_y H_0(k_x, k_y) m_y^\dagger = H_0(k_x, -k_y), \quad (\text{B5})$$

$$m_y H(k_1, k_2) m_y^\dagger = H(k_2, k_1).$$

Mirror symmetry m_x is

$$m_x = \begin{pmatrix} 0 & 0 & 0 & 0 & 0 & 1 \\ 0 & 0 & 0 & 0 & 1 & 0 \\ 0 & 0 & 0 & 1 & 0 & 0 \\ 0 & 0 & 1 & 0 & 0 & 0 \\ 0 & 1 & 0 & 0 & 0 & 0 \\ 1 & 0 & 0 & 0 & 0 & 0 \end{pmatrix}, \quad (\text{B6})$$

$$m_x H_0(k_x, k_y) m_x^\dagger = H_0(-k_x, k_y), \quad (\text{B7})$$

$$m_x H(k_1, k_2) m_x^\dagger = H(-k_2, -k_1).$$

Inversion symmetry I is

$$I_v = \begin{pmatrix} 0 & 0 & 0 & 1 & 0 & 0 \\ 0 & 0 & 0 & 0 & 1 & 0 \\ 0 & 0 & 0 & 0 & 0 & 1 \\ 1 & 0 & 0 & 0 & 0 & 0 \\ 0 & 1 & 0 & 0 & 0 & 0 \\ 0 & 0 & 1 & 0 & 0 & 0 \end{pmatrix}, \quad (\text{B8})$$

$$I_v H(k_x, k_y) I_v^\dagger = H(-k_x, -k_y), \quad (\text{B9})$$

$$I_v H_0(k_1, k_2) I_v^\dagger = H(-k_1, -k_2).$$

Nonsymmorphic symmetry $g_y = \{m_y | \tau_x\}$ is

$$g_y = e^{i(k_x \cos \theta + k_y \sin \theta)} \begin{pmatrix} 0 & 0 & 1 & 0 & 0 & 0 \\ 0 & 1 & 0 & 0 & 0 & 0 \\ 1 & 0 & 0 & 0 & 0 & 0 \\ 0 & 0 & 0 & 0 & 0 & 1 \\ 0 & 0 & 0 & 0 & 1 & 0 \\ 0 & 0 & 0 & 1 & 0 & 0 \end{pmatrix}, \quad (\text{B10})$$

$$g_y H(k_x, k_y) g_y^\dagger = H(k_x, -k_y), \quad (\text{B11})$$

$$g_y H(k_x, k_y) g_y^\dagger = H(k_y, k_x).$$

-
- [1] D. J. Thouless, M. Kohmoto, M. P. Nightingale, and M. den Nijs, *Phys. Rev. Lett.* **49**, 405 (1982).
 [2] P. Streda, *J. Phys. C* **15**, L717 (1982).
 [3] K. v. Klitzing, G. Dorda, and M. Pepper, *Phys. Rev. Lett.* **45**, 494 (1980).
 [4] C. L. Kane and E. J. Mele, *Phys. Rev. Lett.* **95**, 146802 (2005).
 [5] B. A. Bernevig and S.-C. Zhang, *Phys. Rev. Lett.* **96**, 106802 (2006).
 [6] L. Fu and C. L. Kane, *Phys. Rev. B* **76**, 045302 (2007).
 [7] J. E. Moore and L. Balents, *Phys. Rev. B* **75**, 121306(R) (2007).
 [8] M. König, S. Wiedmann, C. Brüne, A. Roth, H. Buhmann, L. W. Molenkamp, X.-L. Qi, and S.-C. Zhang, *Science* **318**, 766 (2007).
 [9] X.-L. Qi, T. L. Hughes, and S.-C. Zhang, *Phys. Rev. B* **78**, 195424 (2008).
 [10] J. E. Moore, *Nature (London)* **464**, 194 (2010).
 [11] M. Z. Hasan and C. L. Kane, *Rev. Mod. Phys.* **82**, 3045 (2010).
 [12] X.-L. Qi and S.-C. Zhang, *Rev. Mod. Phys.* **83**, 1057 (2011).
 [13] A. A. Burkov and L. Balents, *Phys. Rev. Lett.* **107**, 127205 (2011).
 [14] X. Wan, A. M. Turner, A. Vishwanath, and S. Y. Savrasov, *Phys. Rev. B* **83**, 205101 (2011).
 [15] L. Balents, *Physics* **4**, 36 (2011).
 [16] A. M. Turner, A. Vishwanath, and C. O. Head, *Topol. Insul.* **6**, 293 (2013).
 [17] O. Vafek and A. Vishwanath, *Annu. Rev. Condens. Matter Phys.* **5**, 83 (2014).
 [18] H. Weng, C. Fang, Z. Fang, B. A. Bernevig, and X. Dai, *Phys. Rev. X* **5**, 011029 (2015).
 [19] W. A. Benalcazar, B. A. Bernevig, and T. L. Hughes, *Science* **357**, 61 (2017).
 [20] J. Langbehn, Y. Peng, L. Trifunovic, F. von Oppen, and P. W. Brouwer, *Phys. Rev. Lett.* **119**, 246401 (2017).

- [21] J. Noh, W. A. Benalcazar, S. Huang, M. J. Collins, K. P. Chen, T. L. Hughes, and M. C. Rechtsman, *Nat. Photon.* **12**, 408 (2018).
- [22] S. Imhof, C. Berger, F. Bayer, J. Brehm, L. W. Molenkamp, T. Kiessling, F. Schindler, C. H. Lee, M. Greiter, and R. Thomale, *Nat. Phys.* **14**, 925 (2018).
- [23] F. Schindler, Z. Wang, M. G. Vergniory, A. M. Cook, A. Murani, S. Sengupta, A. Y. Kasumov, R. Deblock, S. Jeon, I. Drozdov, H. Bouchiat, S. Guéron, A. Yazdani, B. A. Bernevig, and T. Neupert, *Nat. Phys.* **14**, 918 (2018).
- [24] M. Lin and T. L. Hughes, *Phys. Rev. B* **98**, 241103(R) (2018).
- [25] F. Schindler, A. M. Cook, M. G. Vergniory, Z. Wang, S. S. Parkin, B. A. Bernevig, and T. Neupert, *Sci. Adv.* **4**, eaat0346 (2018).
- [26] L. Fu, *Phys. Rev. Lett.* **106**, 106802 (2011).
- [27] Y. Tanaka, Z. Ren, T. Sato, K. Nakayama, S. Souma, T. Takahashi, K. Segawa, and Y. Ando, *Nat. Phys.* **8**, 800 (2012).
- [28] P. Dziawa, B. Kowalski, K. Dybko, R. Buczko, A. Szczerbakow, M. Szot, E. Łusakowska, T. Balasubramanian, B. M. Wojek, M. Berntsen *et al.*, *Nat. Mater.* **11**, 1023 (2012).
- [29] T. H. Hsieh, H. Lin, J. Liu, W. Duan, A. Bansil, and L. Fu, *Nat. Commun.* **3**, 982 (2012).
- [30] Y. Ando and L. Fu, *Annu. Rev. Condens. Matter Phys.* **6**, 361 (2015).
- [31] J.-X. Zhang, M. C. Rechtsman, and C.-X. Liu, *APL Photonics* **1**, 050803 (2016).
- [32] M. Ezawa, *Phys. Rev. Lett.* **120**, 026801 (2018).
- [33] C. W. Peterson, W. A. Benalcazar, T. L. Hughes, and G. Bahl, *Nature (London)* **555**, 346 (2018).
- [34] M. Serra-Garcia, V. Peri, R. Stüsstrunk, O. R. Bilal, T. Larsen, L. G. Villanueva, and S. D. Huber, *Nature (London)* **555**, 342 (2018).
- [35] W. A. Benalcazar, B. A. Bernevig, and T. L. Hughes, *Phys. Rev. B* **96**, 245115 (2017).
- [36] J. C. Budich, J. Eisert, E. J. Bergholtz, S. Diehl, and P. Zoller, *Phys. Rev. B* **90**, 115110 (2014).
- [37] C. H. Lee, D. P. Arovas, and R. Thomale, *Phys. Rev. B* **93**, 155155 (2016).
- [38] C. H. Lee, M. Claassen, and R. Thomale, *Phys. Rev. B* **96**, 165150 (2017).
- [39] F. K. Kunst, G. van Miert, and E. J. Bergholtz, *Phys. Rev. B* **97**, 241405(R) (2018).
- [40] C.-X. Liu, R.-X. Zhang, and B. K. VanLeeuwen, *Phys. Rev. B* **90**, 085304 (2014).
- [41] S. A. Parameswaran, A. M. Turner, D. P. Arovas, and A. Vishwanath, *Nat. Phys.* **9**, 299 (2013).
- [42] K. Shiozaki, M. Sato, and K. Gomi, *Phys. Rev. B* **91**, 155120 (2015).
- [43] H. Watanabe, H. C. Po, A. Vishwanath, and M. Zaletel, *Proc. Natl. Acad. Sci. U.S.A.* **112**, 14551 (2015).
- [44] L. M. Schoop, M. N. Ali, C. Straßer, A. Topp, A. Varykhalov, D. Marchenko, V. Duppel, S. S. Parkin, B. V. Lotsch, and C. R. Ast, *Nat. Commun.* **7**, 11696 (2016).
- [45] J. Y. Lin, N. C. Hu, Y. J. Chen, C. H. Lee, and X. Zhang, *Phys. Rev. B* **96**, 075438 (2017).
- [46] V. V. Albert, L. I. Glazman, and L. Jiang, *Phys. Rev. Lett.* **114**, 173902 (2015).
- [47] J. Ningyuan, C. Owens, A. Sommer, D. Schuster, and J. Simon, *Phys. Rev. X* **5**, 021031 (2015).
- [48] X.-L. Qi, *Phys. Rev. Lett.* **107**, 126803 (2011).
- [49] C. H. Lee and P. Ye, *Phys. Rev. B* **91**, 085119 (2015).
- [50] S. Kivelson, *Phys. Rev. B* **26**, 4269 (1982).
- [51] N. Marzari and D. Vanderbilt, *Phys. Rev. B* **56**, 12847 (1997).
- [52] R. Yu, X. L. Qi, A. Bernevig, Z. Fang, and X. Dai, *Phys. Rev. B* **84**, 075119 (2011).
- [53] J. K. Asbóth, L. Oroszlány, and A. Pályi, *A Short Course on Topological Insulators*, Lecture Notes in Physics Vol. 919 (Springer, Cham, 2016).
- [54] Alternatively, this topological classification can also be obtained through the mirror Chern number [22], without reference to higher-order polarization.
- [55] L. Li, M. Umer, and J. Gong, *Phys. Rev. B* **98**, 205422 (2018).
- [56] X. Zhang, Y. Chen, Y. Wang, Y. Liu, J. Y. Lin, N. C. Hu, B. Guan, and C. H. Lee, *Phys. Rev. B* **100**, 041110(R) (2019).
- [57] C. H. Lee, G. Li, G. Jin, Y. Liu, and X. Zhang, *Phys. Rev. B* **97**, 085110 (2018).
- [58] T. Helbig, T. Hofmann, C. H. Lee, R. Thomale, S. Imhof, L. W. Molenkamp, and T. Kiessling, *Phys. Rev. B* **99**, 161114(R) (2019).
- [59] Y. Wang, L.-J. Lang, C. H. Lee, B. Zhang, and Y. D. Chong, *Nat. Commun.* **10**, 1102 (2019).
- [60] Y. Lu, N. Jia, L. Su, C. Owens, G. Juzeliūnas, D. I. Schuster, and J. Simon, *Phys. Rev. B* **99**, 020302(R) (2019).
- [61] C. H. Lee, S. Imhof, C. Berger, F. Bayer, J. Brehm, L. W. Molenkamp, T. Kiessling, and R. Thomale, *Commun. Phys.* **1**, 39 (2018).
- [62] T. Hofmann, T. Helbig, C. H. Lee, M. Greiter, and R. Thomale, *Phys. Rev. Lett.* **122**, 247702 (2019).
- [63] L. Li, C. H. Lee, and J. Gong, *Commun. Phys.* **2**, 135 (2019).
- [64] C. H. Lee, L. Li, and J. Gong, *Phys. Rev. Lett.* **123**, 016805 (2019).
- [65] M. Ezawa, *Phys. Rev. B* **99**, 201411(R) (2019).
- [66] M. Ezawa, *Phys. Rev. B* **99**, 121411(R) (2019).
- [67] T. Hofmann, T. Helbig, F. Schindler, N. Salgo, M. Brzezińska, M. Greiter, T. Kiessling, D. Wolf, A. Vollhardt, A. Kabašić *et al.*, *Phys. Rev. Res.* **2**, 023265 (2020).